Title

Nonscattering Waveguides Based on Tensor Impedance Surfaces

Journal

IEEE Transactions on Antennas and Propagation, 63(4)

ISSN

0018-926X

Authors

Quarfoth, Ryan G

Sievenpiper, Daniel F

Publication Date

2015

DOI

10.1109/tap.2015.2401051

Peer reviewed

Nonscattering Waveguides Based on Tensor Impedance Surfaces

Ryan G. Quarfoth, *Student Member, IEEE*, and Daniel F. Sievenpiper, *Fellow, IEEE*

***Abstract*—A tensor impedance surface waveguide is built using anisotropic unit cells. The waveguide can propagate a confined waveguide mode along its axis while waves incident to the guide at an orthogonal direction pass through as if the waveguides were not present. Both straight and curved implementations are demonstrated. Surface waves incident at an angle to the waveguide show reflection and refraction at the impedance interface. A theoretical model for tensor impedance surface waveguides is generalized to include dispersive unit cells and bending loss around curves. Dispersion results for modes propagating in the waveguide show agreement between the theory, simulation, and experimental measurements. A curved waveguide is also constructed which guides surface waves around a curve and is transparent to surface waves incident at an orthogonal angle.**

***Index Terms*—Artificial materials, impedance boundary conditions, impedance sheets, metamaterials, periodic structures, surface impedance, surface waves.**

I. Introduction

IMPEDANCE surfaces are artificially engineered metasurfaces that have been used for multiple applications including waveguides [1]–[3], antennas [4]–[6], lenses [7], [8], and coatings [9], [10]. Impedance surfaces have also been proposed for beam shifting and cloaking applications [11]–[14], and other surfaces with continuously varying properties [15]. At terahertz and optical frequencies impedance-surface-like structures can be created by varying the conductivity of graphene [16], and modeling methods have also been extended to these frequencies [17]. Three-dimensional (3-D) conformal metasurfaces have also been studied [18], along with other types of metasurfaces such as tensor transmission-line metamaterials [19].

Impedance surfaces are advantageous because they can be modeled using a planar impedance boundary condition, which specifies the relation between the electric and magnetic fields. Impedance surfaces can be designed and simulated using the simple boundary condition instead of complex structures, and this allows very large structures to be accurately and quickly modeled. Impedance surfaces, like other metasurfaces and metamaterials, can be created by inserting periodic inclusions into materials [20]. The period of these inclusions must be small compared to the wavelength. Anisotropic surfaces can be modeled using the tensor impedance boundary condition [5]. Multiple unit cell geometries for tensor impedance surfaces using printed circuit structures have been analyzed [21].

Impedances surfaces support surface waves, which are electromagnetic wave mode that can propagate bound to the surfaces. Surface waves are generated on substrates near antennas or due to external radiation and they can damage equipment, degrade antenna patterns, and effect radar scattering. Surface-wave waveguides could be applied to mitigate these issues by allowing precise control of surface wave propagation. These waveguides can also be modulated to create an antenna [4], used to feed antennas or lenses, used to integrate multiple components into a single design, or used as a component in other more complex systems.

Impedance surface waveguides have been theoretically investigated [1], [2], and a surface-wave waveguide has been built and measured [3]. It was also shown in simulation that a surface wave beam can be guided around a curve by rotating the tensor impedance axis and grading the index to align phase fronts of the beam [3]. In this paper, the previous theoretical dispersion model (from [2]) is confirmed experimentally, and a transparent waveguide is built that supports confined waveguide modes but allows surface waves to pass in the orthogonal direction. This setup can reduce coupling between the waveguide mode and external sources. The transparent waveguide is also an example of a structure which can perform two different functions depending on the propagation direction.

In this paper, the impedance surface is built as a printed circuit. These structures are created by patterning metal on the top layer of a grounded dielectric slab. Waveguides can be constructed using impedance surfaces by surrounding a high impedance region with two lower impedance regions. Fig. 1 shows a schematic diagram of an impedance surface waveguide. The waveguide is designed with square and rectangular unit cells as shown in Fig. 2. These unit cells have been analyzed along with their principal axes [22]. Further analysis of printed circuit tensor impedance surfaces has also been performed, and it was found that tensor impedance boundaries do not always accurately model printed structures, and more accurate models have been proposed [23]–[25]. However, currently, these methods can only be applied to individual unit cells, and not large structures like waveguides. In order to confirm the accuracy of the ideal tensor impedance model, we have compared this ideal model to simulations of printed circuit structures and measurement.

Manuscript received November 20, 2013; revised October 22, 2014; accepted December 28, 2014. Date of publication February 06, 2015; date of current version April 03, 2015. This work was supported by Air Force Office of Scientific Research Grant FA9550-10-1-0313 and Grant FA9550-13-1-0014.

R. G. Quarfoth was with the University of California, San Diego, La Jolla, CA 92093 USA. He is now with HRL Laboratories, LLC, Malibu, CA 90265 USA (e-mail: rgquarfoth@hrl.com).

D. F. Sievenpiper is with the University of California, San Diego, La Jolla, CA 92093 USA.

Color versions of one or more of the figures in this paper are available online at http://ieeexplore.ieee.org.

Digital Object Identifier 10.1109/TAP.2015.2401051

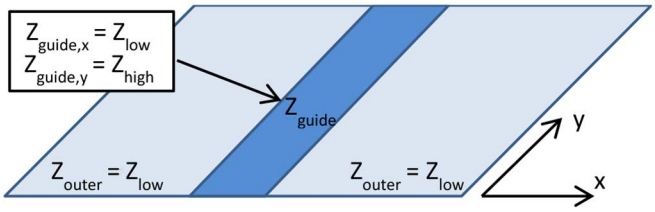

Fig. 1. Model of transparent surface impedance waveguide. A high impedance region is surrounded by two lower impedance regions. Guided surface wave modes can propagate along the higher impedance region. In the opposite direction, the impedance of the guiding and outer regions matches.

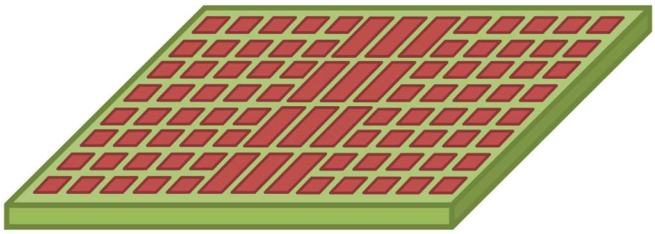

Fig. 2. Physical representation of surface-wave waveguide. A grounded dielectric substrate is patterned with rectangular and square patches. Higher impedance is achieved using the elongated rectangular patches.

Section II reviews the theoretical foundation for impedance surfaces and surface waveguides. The unit cells used to create the surface waveguide are analyzed in Section III. In Section IV, the dispersion of this waveguide is shown to closely match both theory and simulation. Near field measurements are presented in Section V, and it is confirmed that the waveguide supports guided modes as predicted, and is also transparent to a wave traveling in an orthogonal direction. Section VI discusses a curved transparent waveguide which guides waves along a bend. Curved waveguides can suffer bending loss due to the geometry of the discontinuity between high and low impedance regions. Section VII presents an expanded theoretical method that models bending loss and investigates the effect of curve radius and surface impedance on bending loss.

II. Tensor Impedance Waveguide Theory

The tensor impedance boundary condition relates the electric and magnetic fields on a surface [5], [26]. In this paper, the tensor impedance surface is created by patterning metal patches on top of a grounded dielectric substrate and using the fundamental TM-like mode. Tensor impedance surfaces, unlike scalar surfaces, have direction-dependent propagation characteristics [26]. For a specific propagation direction, the tensor impedance can be modeled as a scalar effective surface impedance or as an effective surface index [2, eqs. (9) and (11)]. Using these effective scalar surface properties, a ray optics method was applied that models the dispersion relation of each guided mode of the waveguide [2, eq. (19)]. In this analysis, the impedance surface was assumed to be dispersion free. The realized impedance surfaces have dispersion and the theory must be generalized to allow frequency-dependent impedance as shown below

$$-\left[\frac{\pi m+\varphi\left(\theta,\omega\right)}{d}\right]^{2}+\frac{n_{1}(\theta,\omega)^{2}\omega^{2}}{c^{2}}\sin^{2}\theta=0 \qquad (1)$$

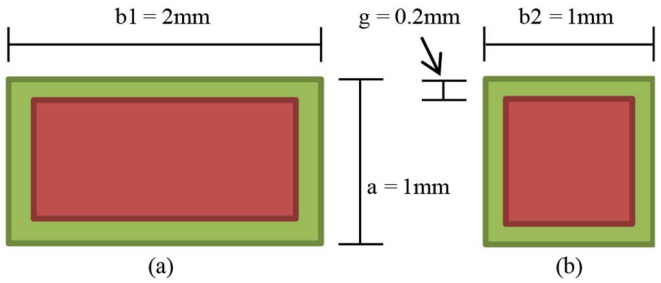

Fig. 3. Unit cell dimensions for (a) anisotropic unit cell and (b) isotropic unit cell. For both unit cells the substrate is a grounded dielectric with a metal patch. The patch is represented by the inner rectangle, and the distance between the patch and the unit cell edge is g = 0.2 mm on all sides. The anisotropic unit cell is of 2 mm × 1 mm and the isotropic unit cell is 1 × 1 mm.

where m is the mode number, $\varphi(\theta,\omega)$ is the phase shift on reflection of the rays in the guide, d is the width of the guide, $n_1(\theta,\omega)$ is the effective surface impedance of the interior region, ω is the angular frequency of the mode, θ is the direction of propagation, and c is the speed of light. The phase shift depends on the index $n(\theta,\omega)$ and impedance $Z(\theta,\omega)$ of the interior and exterior regions of the guide. The surface impedance is frequency-dependent, but while applying the theory, a harmonic excitation is assumed. Therefore, the dispersion relation is solved independently at each frequency, and single impedance tensor is used for each solution.

To apply the theoretical model, the frequency-dependent impedance, $Z(\theta,\omega)$ must be known ahead of time, along with the corresponding index $n(\theta,\omega)$. In this paper, the rotation and frequency dependence of the unit cells are determined by simulation, and these values are applied to the theoretical model. These simulations are described in Section III. Along with frequency dispersion, realized impedance surface exhibits spatial dispersion. This phenomenon has been analyzed for patch-type unit cells with no vias [23], [24]. Spatial dispersion implies an inconsistency between the predicted anisotropy as defined by a tensor impedance surface and the actual anisotropy of the unit cell. This inconsistency causes errors in $Z(\theta,\omega)$ and $n(\theta,\omega)$, but it will be shown in Sections III and IV that ideal theory can still accurately model the waveguide dispersion.

III. Unit Cell Analysis

The substrate for the waveguide unit cells was 1.27 mm Rogers 3010 (for simulations we used the design dielectric constant $\varepsilon_r = 11.2$). This substrate has the highest dielectric constant of commonly available printed circuit board materials and the largest standard thickness. Higher dielectric constants and larger thickness have been shown to allow broader bandwidth anisotropy [21]. The dimensions of the rectangular unit cell for the guiding region are shown in Fig. 3(a), and the isotropic unit cell for the outer region is shown in Fig. 3(b). Both unit cells have gaps between the metal patch and the edge of the unit cell that are identical on all four sides. Surface impedance dispersion was solved in HFSS, and plots are shown in Fig. 4. For the isotropic 1 mm × 1 mm unit cell, the impedance along the two principal axes is identical because the unit cell is square. The 2 mm × 1 mm unit cell has different impedance for each axis.

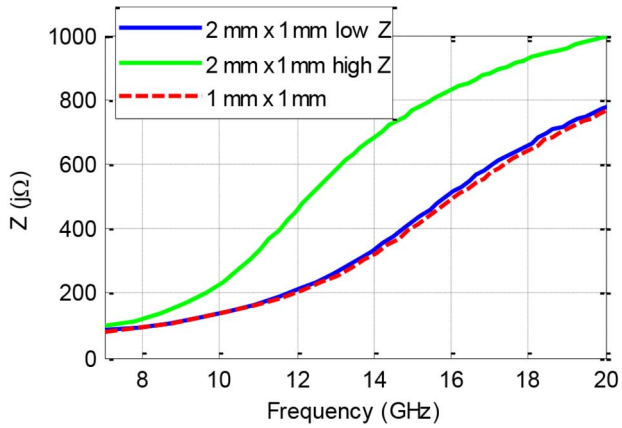

Fig. 4. Surface impedance versus frequency along principal directions of anisotropic and isotropic unit cells. The low impedance direction of the 2 mm × 1 mm unit cell has the same impedance relation as the 1 mm × 1 mm unit cell.

The impedance along the 1 mm dimension of the rectangular cell is nearly identical to the 1 mm × 1 mm unit cell (as also demonstrated in [22]). The fact that the square unit cell and the short direction of the rectangular unit cell have the same surface impedance is what allows the waveguide to be transparent in orthogonal directions. The larger impedance along the propagating direction of the rectangular unit cell allows waveguide modes to be confined to the interior region.

Fig. 4 shows the anisotropic behavior for the principal axes of the 2 mm × 1 mm unit cell, but it is also necessary to verify the performance of the unit cell for waves propagating at directions between the principal axes. For ideal tensor impedance boundary conditions, the dispersion for the principal axes is sufficient to calculate the dispersion at any other angle. However, on realized surfaces, spatial dispersion [23], [24] and mode interference [21] can distort propagation between the principal axes. The dispersion relation for multiple propagation directions has been simulated for both isotropic and anisotropic unit cells. Isofrequency index contours for the isotropic unit cell are shown in Fig. 5(a). For the isotropic unit cell, the contours are circular because the index has the same value for any propagation direction.

Isofrequency contours for the 2 mm × 1 mm unit cell are shown in Fig. 5(b). Results from simulation are plotted as dots. Theoretical curves are shown as solid lines, and are calculated using the results of the principal axis simulations at each frequency. The principal axes are oriented along the x- and y-axes, where the x-axis (high impedance) corresponds to a wave propagating along the 2 mm dimension of the unit cell and the y-axis (low impedance) corresponds to the 1 mm dimension. At low frequencies, the ideal theory and simulation match but as frequency increases the simulation deviates from the theory. The cutoff of the TE mode is at 12.3 GHz, and it has been shown that this is where the ideal tensor impedance theory is no longer valid [21]. Above the cutoff frequency, the simulation rapidly deviates from the theory with the worst estimation generally occurring around a propagation angle of 45°. At 12, 13, 15 GHz, the index is off by 6%, 12%, and 15%, respectively, for a wave propagating at 45°. This error is similar at higher

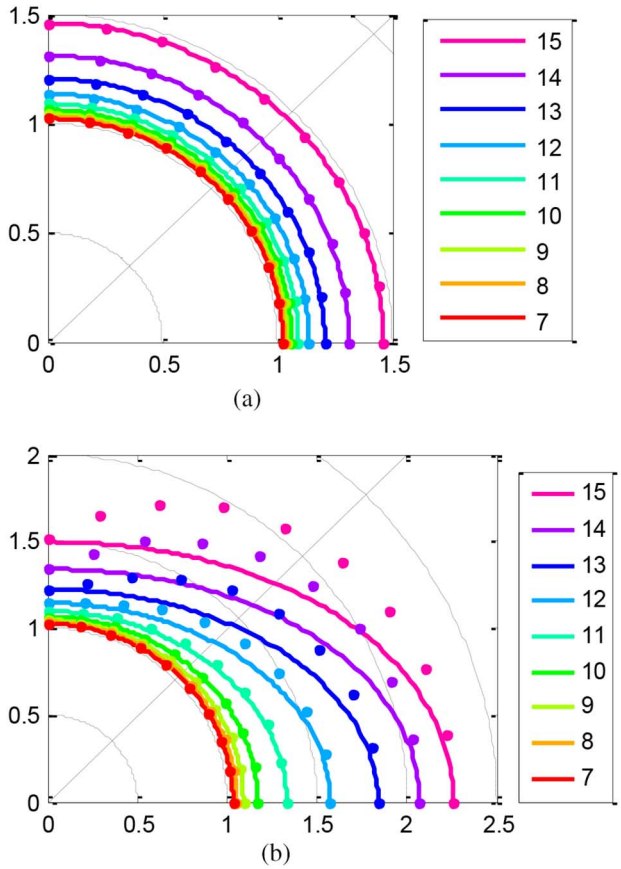

Fig. 5. Isofrequency contours for (a) isotropic unit cell and (b) anisotropic unit cell. The radial direction is effective index and the theta direction is the direction of propagation. Theoretical curves are shown as solid lines and simulations are the dots. The legend labels different frequencies with units of GHz. The contours are symmetric across the x- and y-axis so only the first quadrant is plotted. Ten rotations from 0° to 90° are simulated.

frequencies but other angles begin to have large error also due to mode distortion.

Although, the unit cell dispersion curve deviates from the simple single-mode theory, especially above the TE cutoff at 12.3 GHz, the guide is oriented along the principal axis of the unit cell. In this orientation, the wave is propagating along the direction that does not deviate as significantly from the theory. In Section IV, it is found in both simulation and experiment that the waveguide operates above 12.3 GHz consistently with impedance surface theory.

IV. Waveguide Mode Dispersion and Fields

The dispersion of a waveguide is tested using measurement, simulation, and theoretical model. For each case, the width of the waveguide is set to $d = 10$ mm. In general, wider guides bend the dispersion relation to lower frequencies, and lower the cutoff frequency of higher order waveguide modes.

A. Measured Dispersion Setup

A surface-wave waveguide was constructed using the unit cells analyzed in Section III. The total size of the board was 16 × 10 inches and the waveguide was 16 inches long centered

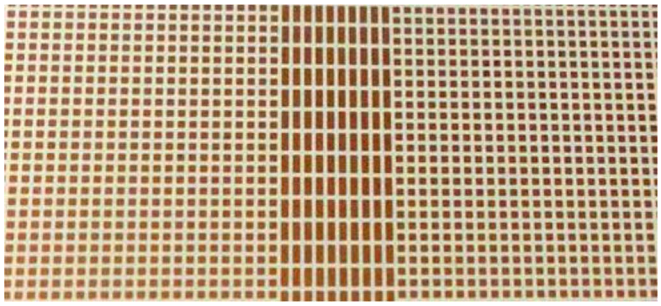

Fig. 6. Photograph of tensor impedance surface waveguide.

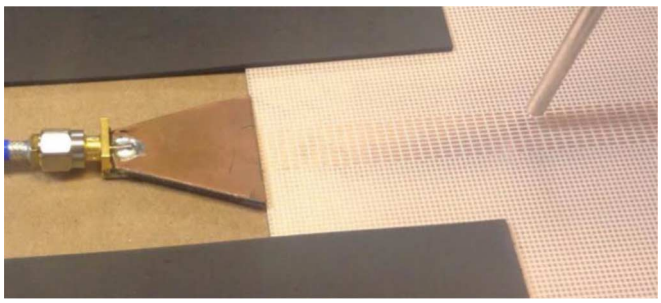

Fig. 7. Measurement setup for waveguide. Magnetic absorbers are place to the sides of a trapezoidal feed. A vertical probe is located in the upper right side of the photograph.

on the board with a 10-mm wide guiding region (10 unit cells wide). A photograph of a section of the waveguide is shown in Fig. 6. A near field scanner was used to make the dispersion measurement. The dispersion was obtained from the phase velocity of the mode in the waveguide. The measurement setup is shown in Fig. 7. The feed is a trapezoidal sheet of Rogers 5880. An end-launch SMA adapter is attached to the back of the feed and leads to one port of an Agilent E5071C Vector Network Analyzer (VNA). The second port of the VNA is attached to a probe that is scanned across the surface. The probe tip is 5 mm long and oriented vertically approximately 2 mm above the surface. For dispersion measurements, the probe is scanned along the center of the guide at $200\,\mu$m increments. At each position, S21 phase is measured by the VNA, and this data is used to calculate the phase velocity. The effective surface index is calculated from the phase velocity, and this index is used to derive the dispersion of the waveguide.

The feed does not couple perfectly into the guided surface mode and some power is reflected or launched as surface waves in the outer region. However, waves excited into a guided mode do not spill outside the guiding region, and the feed is designed so that minimal fields are excited outside of the waveguide mode at the center of the operating region. For printed circuit structures, other surface wave excitations have been used such as a Yagi-like surface wave launcher [27], [28] and a flared microstrip line [4], [29]. These could allow better coupling efficiency into the waveguides. However, for this study, the discrete trapezoidal surface wave launcher allowed the convenience of moving the feed to launch a guided wave, or to launch waves at other positions or angles on the surface. Two sheets of magnetic absorber (Arc-Tec DD11006) were placed on either side of the feed to limit the amount of power reflected back into the guide from the outer region. Both TM and TE modes are absorbed, and the modes are dissipated both above and within the substrate. Magnetic absorber is also used to terminate the guided mode and prevent reflections back into the guide. A well-matched surface wave launcher could also be used to terminate the mode into a 50-Ω load.

B. Simulated Dispersion Setup

The dispersion of the waveguide was simulated using the eigenmode solver in Ansys HFSS version 15. The model used ideal tensor impedance boundary conditions. Because of dispersion in the realized surface, the impedances are set differently for each frequency as stipulated in Fig. 4. The simulation setup is described in [2, Section V], except this paper uses the anisotropic impedance boundary condition (instead of the checkerboard structure), which has been implemented in the HFSS eigenmode solver in the time since the previous publication. The waveguide simulation was performed over the range where the unit cell was simulated: 7–20 GHz (as seen in Fig. 4). The impedance data were interpolated to obtain the values at 1 GHz increments.

C. Theoretical Dispersion

The theoretical dispersion relationship is described by (1) and fully derived in [2]. As noted in Section II, the impedance of the unit cell must be solved before the theoretical dispersion can be solved, and this impedance is dependent on both frequency and propagation direction. The impedance relation for the principal axes is shown in Fig. 4. Even though the guided wave travels along the principal axes of the impedance tensor, the impedance at intermediate angles must be known to correctly apply the ray optics theory. For intermediate angles, the impedance values were obtained using two different methods (each plotted in Fig. 5). The first method used simulated impedances for the principal directions and derived other angles by assuming an ideal tensor impedance boundary. The second method used simulated values from each of the intermediate angles exactly. Both methods are compared to measurement and simulation in the following section.

D. Dispersion Results

The results for each dispersion method are shown in Fig. 8. The measured dispersion closely matches simulation and theory. Only the lowest mode can be measured, and the results stop at 15 GHz. Above this frequency, data are difficult to obtain. At higher frequencies, the impedance of the unit cells goes up and waves are more tightly bound to the surface. The measurement probe is scanned 2 mm above the surface, and if significant wave power is located below this height it becomes difficult to obtain an accurate measurement. Also, at higher frequencies, higher order guided modes are supported and dual mode operation occurs. In the fabricated structure, the second-order mode is predicted by theory at 14.5 GHz. When two (or more) modes

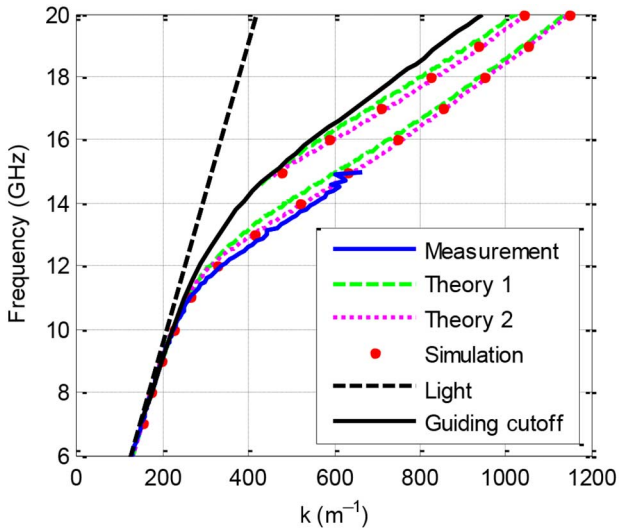

Fig. 8. Dispersion relation for guided modes in tensor impedance surface waveguide. Only the lowest mode can be measured and this is shown as a solid line. The first two modes are shown as dashed lines for the theoretical solutions, and as dots for simulation. The first theory curve uses ideal tensor impedance theory to obtain impedance at intermediate angles and the second theory curve uses simulation to get these values. A black dashed line is the dispersion of light in a vacuum. Guided modes must lie below the dispersion relation of the outer region, and this is shown as a black line.

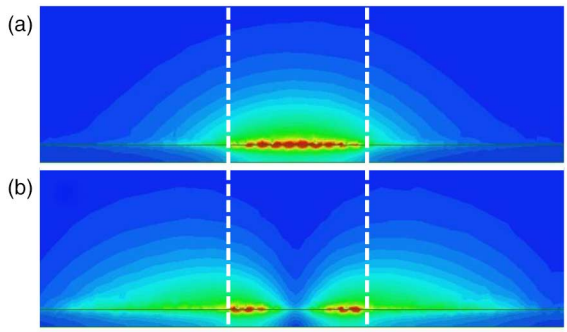

Fig. 9. Normalized electric field magnitude at 12 GHz for (a) first mode and (b) second mode for a simulation of a surface waveguide.

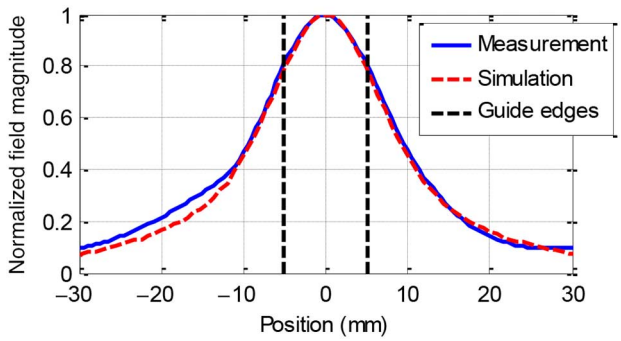

Fig. 10. Normalized electric field magnitude above waveguide.

are present, it becomes difficult to determine the phase velocity of any single mode due to interference between the modes. In simulation and theory, single-mode operation can be strictly enforced.

Simulated and theoretical curves are shown up to 20 GHz for the first two guided modes. The second mode has a cutoff when it intersects the dispersion curve of the outer region. Two theoretical methods were used as described in the previous section. The maximum difference in frequency between the two theories is less than 0.4 GHz for either mode ($<3\%$). Therefore, results show that the simplified theory assuming an ideal tensor impedance boundary is sufficient to predict the approximate dispersion relation. The second method using the simulated impedances is slightly more accurate, but requires many more simulations.

E. Field Profile of Guided Mode

The fields for the guided mode were measured and compared to simulation. The fields for ideal impedance boundary conditions were shown in [2]. A dispersive structure using the rectangular unit cells is analyzed here. The model is constructed identically to the experimental model with 10 unit cells across guiding region and 50 unit cells on across the isotropic region on each side. The electric field magnitude is shown for the first two guided modes in Fig. 9. The guiding region is marked as a dashed line, and the mode is propagating into the page with exponential field decay above the surface.

Using the same experimental setup as for dispersion, a probe was scanned across the guide orthogonal to the direction of propagation. The probe was placed 2 mm above the surface and measurements were taken at 200 μm increments. The normalized field magnitude is plotted in Fig. 10, along with an equivalent line from the simulation. Within the guided region, the simulated and measured responses are nearly identical and have a sinusoidal profile. Outside the guide, the field decays exponentially with distance. The minor differences in field magnitude are likely due to the energy excited outside the guide. Only the first mode can be measured in this manner because a pure second mode cannot be experimentally excited. The impedance contrast between regions affects the confinement of the mode with larger contrasts more closely confining modes to the guiding region. Wider guides also have more mode confinement.

V. Near Field Measurements

Two-dimensional (2-D) near field measurements were obtained using the same waveguide and experimental setup as in Section IV. The total size of the surface was 10×16 inches. The measured area is slightly smaller than the total board size to allow space for the feed and absorbers around the edge of the surface. The excitation source, shown in Fig. 7, does not couple perfectly into guided modes at all frequencies, and some power is excited directly to the outer region. A vertical probe was swept 5 mm above the surface along a 2-mm grid. The probe was scanned higher above the surface for 2-D field measurements because the surface was not completely flat and scanning lower could cause contact between the probe and surface at the edges. For each measurement, about 25,000 points are obtained, and normalized field results at 11 GHz are shown in Fig. 11.

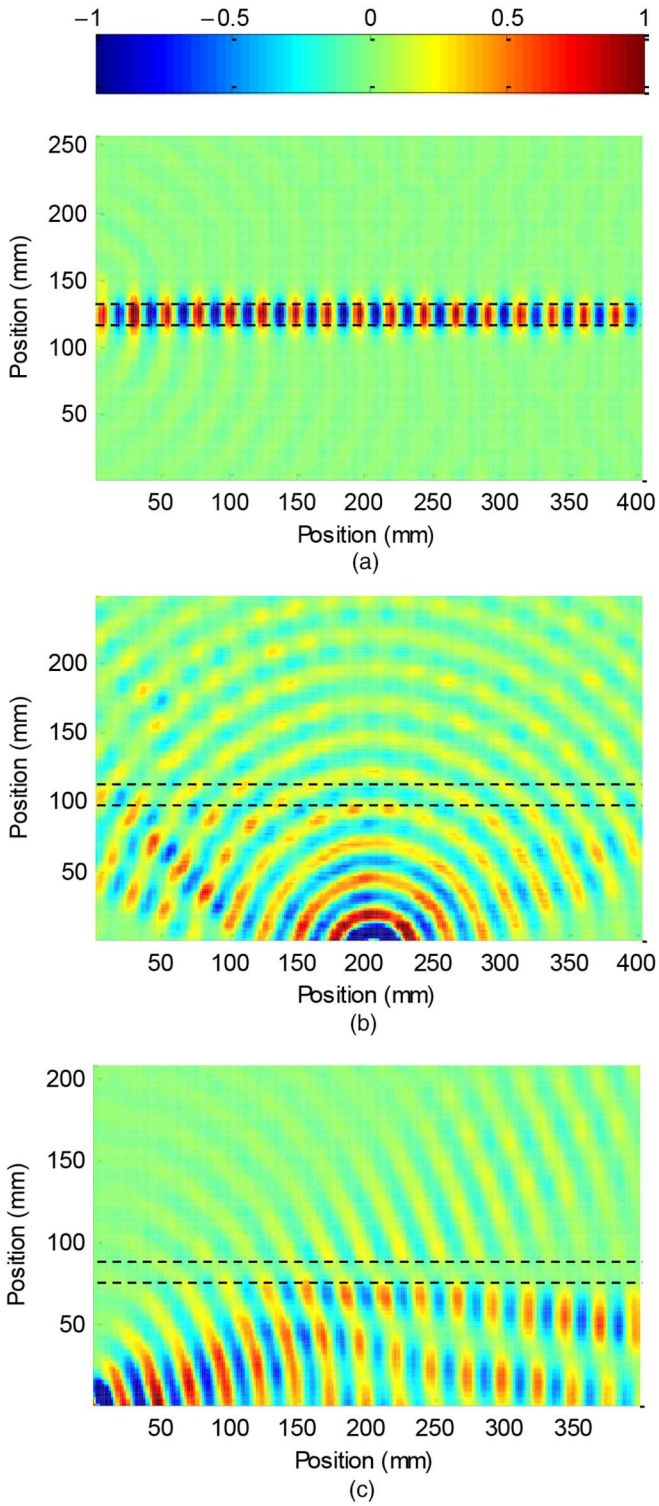

Fig. 11. Measured normalized vertical (out of page) electric field at 11 GHz for (a) guided mode; (b) orthogonal mode; and (c) angled mode. Fields in (a)–(c) are not plotted to the same scale.

A guided mode is displayed in Fig. 11(a). The mode is bound near the guide and does not leak to the outer region. The measured bandwidth for guided modes is from 9.4 to 15.2 GHz. Below 9.4 GHz, the measured mode is a regular surface wave (not confined to the guiding region) because the impedance inside and outside the guide is almost identical. At 11 GHz, as shown in Fig. 11(a), almost all of the fields are in the waveguide mode and minimal fields are present in the outer region. Above 14 GHz, the source excites more measurable fields in the outer region than as a guided mode. This is because higher frequency modes have high impedance. High impedance modes are tightly bound to the surface, and this is difficult to measure because the probe is scanned 5 mm above the surface (in order to avoid scratching the material). At higher frequencies, modes excited in the outer region (which still has lower impedance) are measured much more easily because they are not as tightly bound. These outer region modes can reflect off the edges of the board and travel back across the waveguide making it difficult to isolate the guided mode which exists mostly below the probe. However, power that does enter as a guided mode does not leak away from the guide.

Fig. 11(b) shows a 2-D field plot for a surface with a feed located in the exterior region. The feed was a vertically oriented monopole that excited semicircular phase fronts on the surface. The guiding and outer regions have identical surface impedance for surface waves incident normal to the guide. Therefore, as seen in Fig. 11(b), waves at normal incidence pass through the guide as if it was not present, and transparency is confirmed. In this case, the wave front is only orthogonal directly above the source. At off-normal angles, some reflections and distortion can be seen off the guide. In Fig. 11(c), the trapezoidal feed is used to launch a surface wave toward the waveguide at a small grazing angle. In this case, the higher impedance guiding region reflects a significant portion of the incident power.

VI. Curved Waveguide

A transparent curved waveguide was designed and measured, and Fig. 12(a) illustrates a schematic diagram for the surface. The outer region has small isotropic surface impedance, analogous to Fig. 1, and the guiding region is curved around a point located at the corner of the structure. The guiding region has anisotropic impedance with the radial direction equal to the outer region. The high impedance direction is along the angular dimension of the guide. The design supports guided waves along curve, and waves traveling from a point source at the center of curvature pass across the guiding region without reflection or alteration.

A photograph of a section of the fabricated guide design is shown in Fig. 12(b). The outer region unit cells are identical to those in the straight design (shown in Fig. 3). The anisotropic unit cells are distorted slightly due to the curvature. The design stipulates 2 mm unit cell length along the guiding direction. The unit cells are constructed such that they all have the same angular length, and the unit cell length at the radial center of the guide is set to exactly 2 mm. On the inner edge of the guide, the side length is 1.98 mm. Similarly, on the outer edge, the side length is 2.02 mm. Below 20 GHz, simulation shows that the deviation from the surface impedance of a 2-mm-long unit cell is less than 1%. All unit cells are exactly 1 mm in the radial direction. For the outer region, the unit cells form a 1 mm $\times$ 1 mm grid. These unit cells are removed in the region where the guiding region intersects. As seen in Fig. 12(b), unit cells near

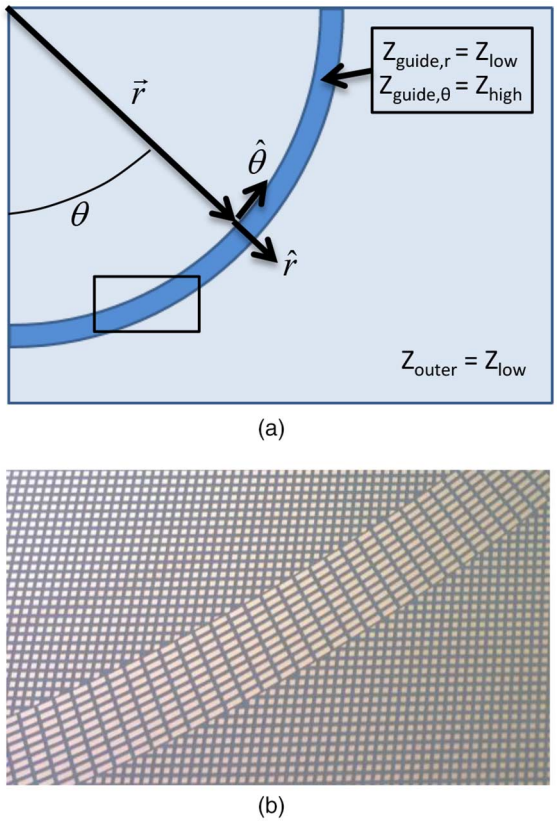

Fig. 12. Curved waveguide diagrams. (a) Schematic of the waveguide dimensions and impedance is shown. (b) Photograph of the fabricated waveguide. The rectangular box in (a) is the location of the photographed region shown in (b).

the edge of the guide are cut so there is no overlap between unit cells.

The width of the guiding region is 10 mm, as was the case for the straight waveguide. The radius from the center of curvature to the center of the waveguide was 20.32 cm. The substrate material and dimensions are the same as before, and near field measurements were obtained from the same system used for the straight waveguides. The guided mode was fed using the straight waveguide as a source. The trapezoidal feed shown in Fig. 7 fed the straight waveguide on one end, and the opposite was pressed up to the curved waveguide. Fig. 13(a) shows a guided mode at 11 GHz. This was the frequency that had the best match between the trapezoidal feed and straight waveguide mode. However, for the curved case, the guided mode leaks into the outer region. Fig. 13(b) shows the same structure at 12 GHz. In this case, there is minimal leakage from the guided mode. Simulation also agrees that there is no leakage into radiated modes or into surface modes outside the waveguide at this frequency. The measured bandwidth for guiding without leakage is from 11.7 to 15 GHz. Bending losses are analyzed in Section VII.

The curved waveguide was also measured at an orthogonal direction. A vertical probe was set at the center of curvature of the guide which is located at the corner of the surface. Magnetic absorber is placed along the edges of the surface to ensure that there are no reflections back into the surface. The source radiates circularly from the center of curvature of the guide such

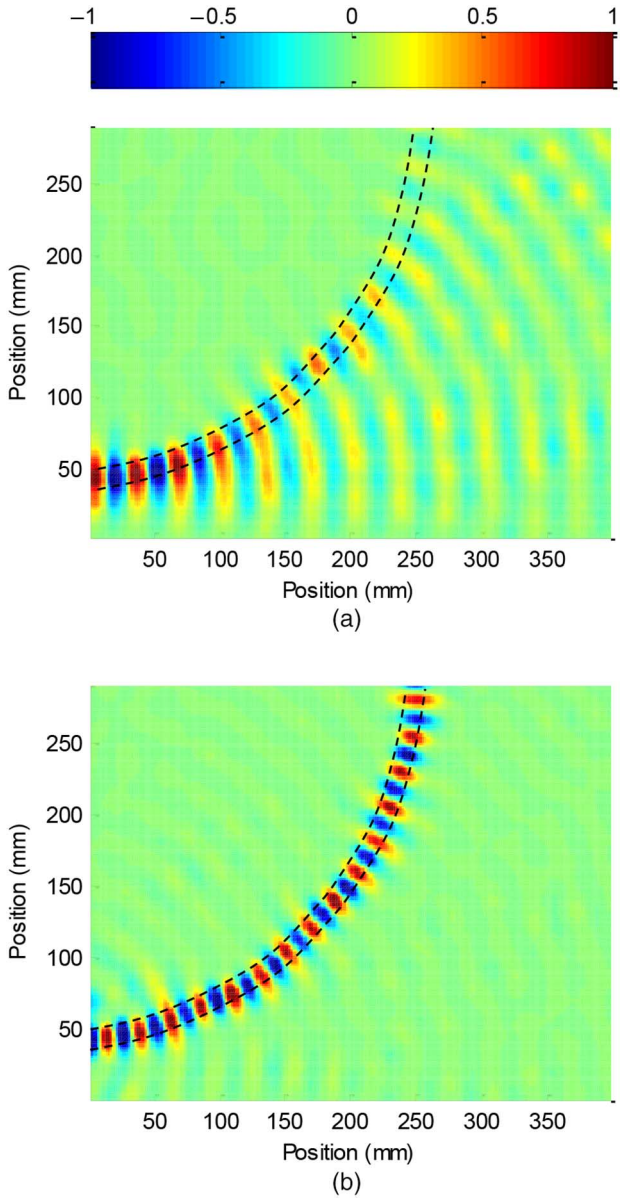

Fig. 13. Measured normalized electric field for guided mode at (a) 11 GHz and (b) 12 GHz. Fields in (a) and (b) are not plotted to the same scale.

that the wave is incidentally normal to the guide across the entire structure. The field plot at 12 GHz is shown in Fig. 14. The wave passes through without reflection confirming again the transparency of the guided region. The fields along the edges are reduced because magnetic absorber is placed along these sides.

VII. Analysis of Bending Losses

As mentioned in Section VI and seen in Fig. 13, the curved waveguide exhibits bending loss that depends on the frequency, waveguide dimensions, and surface properties. This phenomenon also occurs for bending of dielectric slab and fiber structures [30]. Leakage occurs at bends because the mode on the exterior of the curve must travel faster than at the center in order to stay in phase. Leakage occurs where this speed is larger than what can be supported by the materials. Ray optics has

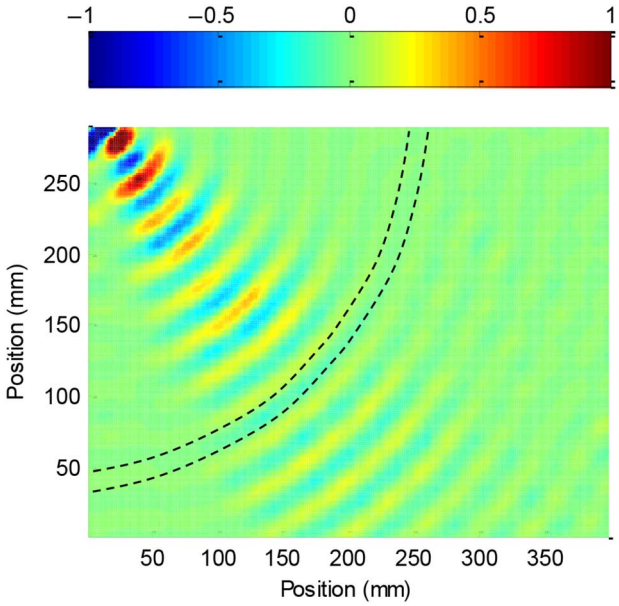

Fig. 14. Measured normalized vertical electric field at 12 GHz for normally incident mode.

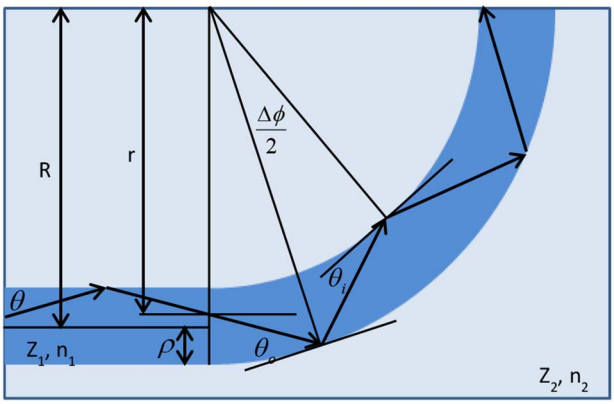

Fig. 15. Setup for ray optics analysis of curved waveguide.

been used to analyze dielectric slab waveguides and fibers to determine the bending loss of a multimode structure [31]–[34]. This method can be adapted for the surface-wave waveguide in order to predict the bending loss due to radiation from a curved waveguide.

For straight waveguides, the ray optics guiding condition dictates that the rays exhibit total internal reflection at the interface between the guiding region and the outer region. This total internal reflection is frustrated by bending, and curved waveguides never exhibit total internal reflection [33]. However, the bending loss can be negligible depending on the setup of the waveguide. The setup for the curved waveguide analysis is shown in Fig. 15. A straight waveguide of width 2ρ feeds a curved waveguide with the same width and surface properties. The dispersion relation of this straight waveguide is solved using (1), and the incidence angle of the ray in the straight waveguide θ is obtained from this equation. The curved waveguide has a center radius of R. The height of the ray crossing between the straight and curved sections is r. The incidence angle at the inner and outer dimensions can be obtained geometrically as follows [34]:

$$\theta_i = \cos^{-1}\left(\frac{r}{R-\rho}\cos\theta\right) \tag{2}$$

$$\theta_o = \cos^{-1}\left(\frac{r}{R+\rho}\cos\theta\right). \tag{3}$$

The incidence angle on the outer surface is always larger than on the inner surface. Rays only lose power on the outer surface, and losses on the inner surface are negligible [33]. The angular dimension of the guide is ϕ, and $\Delta\phi$ is the angular length between successive reflections on the outer diameter.

For incidence onto the outer diameter, the transmission for refracting rays ($\theta_o > \theta_c$) and tunneling rays ($\theta_o < \theta_c$) are shown below:

$$T_R = 4\frac{\sin\theta_o}{\sin\theta_c}\sqrt{\frac{\sin^2\theta_o}{\sin^2\theta_c}-1} \tag{4}$$

$$T_T = 4\frac{\sin\theta_o}{\sin\theta_c}\sqrt{1-\frac{\sin^2\theta_o}{\sin^2\theta_c}} \times \exp\left(\frac{4\pi}{3\lambda}n_1\left(R+\rho\right)\left(\theta_c^2-\theta_o^2\right)^{3/2}\right) \tag{5}$$

$$\theta_c\left(\theta,\omega\right) = \cos^{-1}\left(n_2/n_1\left(\theta,\omega\right)\right) \tag{6}$$

where θ_c is the complement to the critical angle [34].

Note that the critical angle θ_c is explicitly defined to be angle- and frequency-dependent due to the angle- and frequency-dependent index in the guiding region. For refracting rays, T_R is the standard Fresnel relation. For tunneling rays, T_T is solved using a local plane wave analysis [33]. In [2], it was found that a true surface wave Fresnel equation gave improved results for the phase on total internal reflection because it was necessary to calculate the exact reflection phase shift [2, eq. (18)]. For losses due to bending, we have found that local plane wave analysis adequately predicts losses for the curved surface-wave waveguide for large guide radii relative to the wavelength.

Power dissipates due to the transmission out of the waveguide. The attenuation coefficient is the amount of power transmitted T per unit angle between transmissions: $\gamma = T/\Delta\phi$. Power dissipates exponentially as a function of the angular size of the waveguide. The dissipation is calculated by integrating over each incidence height r

$$P\left(\phi\right) = \int_{R-\rho}^{R+\rho} P_0 \exp\left(-\gamma\phi\right) dr \tag{7}$$

where P_0 is the initial power. In multimode fibers, solved in [33], the incident angle θ must also be integrated. This is not necessary for surface-wave waveguides because we assume a single mode whose incident angle can be calculated from (1). This method can be used to solve for geometries with varying curvature as long as the incidence angle is appropriately solved and integrated.

Fig. 16 shows the results for bending loss in the fabricated structure (the plot shows the ratio of power remaining in the

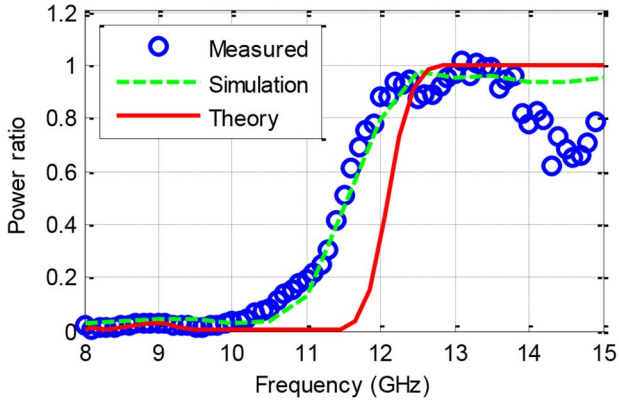

Fig. 16. Ratio of power remaining to total power incident for a 90° bend.

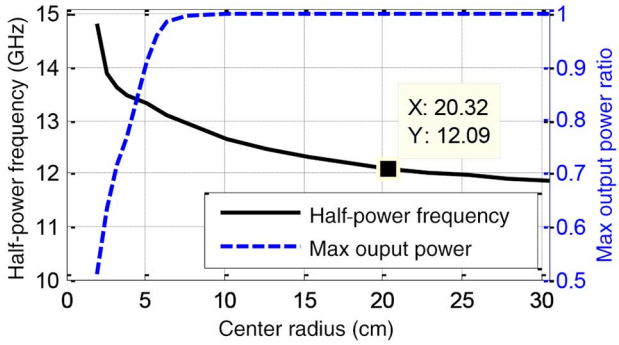

Fig. 17. Frequency of half-power loss versus center radius of the waveguide. The right axis shows the maximum power output from the waveguide.

guide to total power after a 90° bend). The measured data are calculated from the fields above the waveguide. The simulated curve uses ideal tensor impedance boundaries with impedances as shown in Fig. 4 (the simulated curves were also applied and gave similar results). The theory curved is solved numerically from (7). Results show similar characteristics for all three methods. In each case, minimal power is transmitted at low frequencies. At high frequencies, there is nearly full power transmission for the simulated and theory cases. The measured version shows some losses between 14 and 15 GHz. These losses are due to bending loss of the second waveguide mode (which has a theoretical cutoff of 14.2 GHz and is not included in the theory) and material loss. Bending loss of the first mode does not occur in this frequency range. This lossy section is also in the range where the TM mode is distorted by the presence of TE modes. The theoretical model closely predicts the frequency at which the structure no longer has nearly complete guiding at 12.5 GHz. However, the theory shows a steeper drop-off from nearly complete guiding toward increased bending loss at lower frequencies.

The theory was used to predict the bending loss for different waveguide radii using the same unit cells, and the results are shown in Fig. 17. The half-power frequency is the frequency where the guide delivers half the power around the bend. The theory predicts this location at 12.09 GHz for the fabricated structure as seen in Fig. 16 and labeled explicitly in Fig. 17. As the center radius R decreases the half-power frequency increases. This is because higher frequencies have

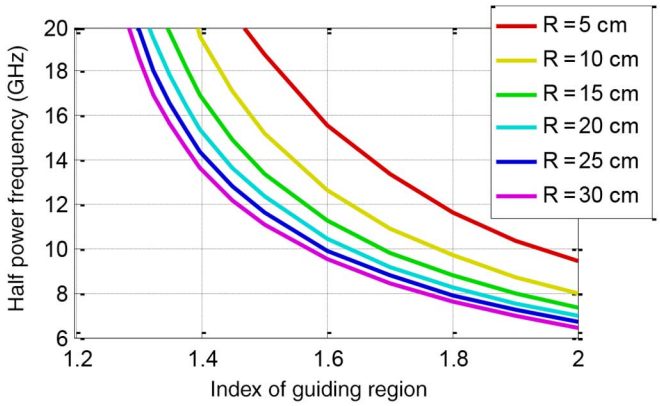

Fig. 18. Half-power frequency versus index of guiding region for multiple center radii. The index of the outer region is 1.1, the guide width is 10 mm, and the bend angle is 90°.

larger impedance contrast, and R is electrically larger. On the right y-axis, the maximum transmitted power is plotted for each R. For $R < 0.75$ cm, the waveguide does not propagate 50% of the power at any frequency. The maximum power output occurs about 0.5 GHz above the half-power frequency as seen in Fig. 16.

In the realized structure, the impedance of the unit cell is dependent on frequency. In order to show the effects of impedance and radius on propagation independently, the theory was applied to a waveguide using ideal impedance boundary conditions. The setup had guide width of 10 mm, and outer region $\mathrm{n} = 1.1$. The index of the inner region was swept from 1.2 to 2 (isotropic) for multiple radii. The results are shown in Fig. 18. For any given index value, increasing the radius decreases the frequency where half the power is transmitted. Similarly, for a specific radius, increasing the index decreases the frequency of half-power transmission.

VIII. Conclusion

We have demonstrated a simple application of tensor impedance surfaces in the form of a waveguide that is transparent to surface waves in the orthogonal direction. This can be extended to enable new applications such as antennas with reduced scattering or nulls in a given direction, or that produce different radiation patterns depending on the feed location.

References

[1] R. Quarfoth and D. Sievenpiper, "Impedance surface waveguide theory and simulation," in *Proc. IEEE Int. Symp. Antennas Propag. (APSURSI)*, 2011, pp. 1159–1162.

[2] R. Quarfoth and D. Sievenpiper, "Artificial tensor impedance surface waveguides," *IEEE Trans. Antennas Propag.*, vol. 61, no. 7, pp. 3597–3606, Jul. 2013.

[3] D. Gregoire and A. Kabakian, "Surface-wave waveguides," *IEEE Antennas Wireless Propag. Lett.*, vol. 10, pp. 1512–1515, Dec. 2011.

[4] A. M. Patel and A. Grbic, "A printed leaky-wave antenna based on a sinusoidally-modulated reactance surface," *IEEE Trans. Antennas Propag.*, vol. 59, no. 6, pp. 2087–2096, Jun. 2011.

[5] B. H. Fong, J. S. Colburn, J. J. Ottusch, J. L. Visher, and D. F. Sievenpiper, "Scalar and tensor holographic artificial impedance surfaces," *IEEE Trans. Antennas Propag.*, vol. 58, no. 10, pp. 3212–3221, Oct. 2010.

[6] G. Minatti, S. Maci, P. De Vita, A. Freni, and M. Sabbadini, "A circularly-polarized Isoflux antenna based on anisotropic metasurface," *IEEE Trans. Antennas Propag.*, vol. 60, no. 11, pp. 4998–5009, Nov. 2012.
[7] M. Bosiljevac, M. Casaletti, F. Caminita, Z. Sipus, and S. Maci, "Nonuniform metasurface Luneburg lens antenna design," *IEEE Trans. Antennas Propag.*, vol. 60, no. 9, pp. 4065–4073, Sep. 2012.
[8] A. Dhouibi, S. N. Burokur, A. de Lustrac, and A. Priou, "Compact metamaterial-based substrate-integrated Luneburg lens antenna," *IEEE Antennas Wireless Propag. Lett.*, vol. 11, pp. 1504–1507, Dec. 2012.
[9] W. Qi, C. P. Scarborough, D. H. Werner, E. Lier, and X. Wang, "Design synthesis of metasurfaces for broadband hybrid-mode horn antennas with enhanced radiation pattern and polarization characteristics," *IEEE Trans. Antennas Propag.*, vol. 60, no. 8, pp. 3594–3604, Aug. 2012.
[10] W. Qi *et al.*, "A Ku-band dual polarization hybrid-mode horn antenna enabled by printed-circuit-board metasurfaces," *IEEE Trans. Antennas Propag.*, vol. 61, no. 3, pp. 1089–1098, Mar. 2013.
[11] R. Quarfoth and D. Sievenpiper, "Anisotropic surface impedance cloak," in *Proc. IEEE Antennas Propag. Soc. Int. Symp. (APSURSI)*, 2012, pp. 1–2.
[12] R. Quarfoth and D. Sievenpiper, "Surface wave scattering reduction using beam shifters," *IEEE Antennas Wireless Propag. Lett.*, vol. 13, pp. 963–966, May 2014.
[13] A. M. Patel and A. Grbic, "Transformation electromagnetics devices based on printed-circuit tensor impedance surfaces," *IEEE Trans. Microw. Theory Tech.*, vol. 62, no. 5, pp. 1102–1111, May 2014.
[14] R. C. Mitchell-Thomas, T. M. McManus, O. Quevedo-Teruel, S. A. R. Horsley, and Y. Hao, "Perfect surface wave cloaks," *Phys. Rev. Lett.*, vol. 111, p. 213901, Nov. 19, 2013.
[15] S. Maci, G. Minatti, M. Casaletti, and M. Bosiljevac, "Metasurfing: Addressing waves on impenetrable metasurfaces," *IEEE Antennas Wireless Propag. Lett.*, vol. 10, pp. 1499–1502, Jan. 2012.
[16] A. Vakil and N. Engheta, "Transformation optics using graphene," *Science*, vol. 332, pp. 1291–1294, 2011.
[17] A. Gholipour, R. Faraji-Dana, G. A. E. Vandenbosch, and S. Safavi-Naeini, "Surface impedance modeling of plasmonic circuits at optical communication wavelengths," *J. Lightwave Technol.*, vol. 31, pp. 3315–3322, Oct. 15, 2013.
[18] D. J. Gregoire, "3-D conformal metasurfaces," *IEEE Antennas Wireless Propag. Lett.*, vol. 12, pp. 233–236, Feb. 2013.
[19] G. Gok and A. Grbic, "Tensor transmission-line metamaterials," *IEEE Trans. Antennas Propag.*, vol. 58, no. 5, pp. 1559–1566, May 2010.
[20] C. L. Holloway *et al.*, "An overview of the theory and applications of metasurfaces: The two-dimensional equivalents of metamaterials," *IEEE Antennas Propag. Mag.*, vol. 54, no. 2, pp. 10–35, Apr. 2012.
[21] R. Quarfoth and D. Sievenpiper, "Unit cell for highly-anisotropic tensor impedance surface," *IEEE Trans. Antennas Propag.*, vol. 62, pp. 4143–4152, 2014.
[22] R. Quarfoth and D. Sievenpiper, "Simulation of anisotropic artificial impedance surface with rectangular and diamond lattices," in *Proc. IEEE Int. Symp. Antennas Propag. (APSURSI)*, 2011, pp. 1498–1501.
[23] A. M. Patel and A. Grbic, "Modeling and analysis of printed-circuit tensor impedance surfaces," *IEEE Trans. Antennas Propag.*, vol. 61, no. 1, pp. 211–220, Jan. 2013.
[24] A. M. Patel and A. Grbic, "Effective surface impedance of a printed-circuit tensor impedance surface (PCTIS)," *IEEE Trans. Microw. Theory Tech.*, vol. 61, no. 4, pp. 1403–1413, Apr. 2013.
[25] A. M. Patel and A. Grbic, "The effects of spatial dispersion on power flow along a printed-circuit tensor impedance surface," *IEEE Trans. Antennas Propag.*, vol. 62, no. 3, pp. 1464–1469, Mar. 2014.
[26] H. J. Bilow, "Guided waves on a planar tensor impedance surface," *IEEE Trans. Antennas Propag.*, vol. 51, no. 10, pp. 2788–2792, Oct. 2003.
[27] H. F. Hammad, Y. M. M. Antar, A. P. Freundorfer, and S. F. Mahmoud, "Uni-planar CPW-fed slot launchers for efficient TM0 surface-wave excitation," *IEEE Trans. Microw. Theory Tech.*, vol. 51, no. 4, pp. 1234–1240, Apr. 2003.
[28] S. K. Podilchak, A. P. Freundorfer, and Y. M. M. Antar, "Planar surface-wave sources and metallic grating lenses for controlled guided-wave propagation," *IEEE Antennas Wireless Propag. Lett.*, vol. 8, pp. 371–374, Jan. 2009.
[29] D. J. Gregoire, "Conformal surface wave feed," U.S. Patent 20,130,285,871, 2013.
[30] E. A. J. Marcatili, "Bends in optical dielectric guides," *Bell Syst. Tech. J.*, vol. 48, pp. 2103–2132, 1969.
[31] A. W. Snyder, "Generalised Fresnel's law for loss due to curvature," *Electron. Lett.*, vol. 9, pp. 609–610, 1973.
[32] A. W. Snyder and D. J. Mitchell, "Bending losses of multimode optical fibres," *Electron. Lett.*, vol. 10, pp. 11–12, 1974.
[33] A. W. Snyder and J. Love, *Optical Waveguide Theory*, vol. 190. New York, NY, USA: Springer, 1983.
[34] M. Remouche, R. Mokdad, A. Chakari, and P. Meyrueis, "Intrinsic integrated optical temperature sensor based on waveguide bend loss," *Opt. Laser Technol.*, vol. 39, pp. 1454–1460, Oct. 2007.

Ryan G. Quarfoth (S'11) received the B.S. degree in engineering (with high distinction) from Harvey Mudd College, Claremont, CA, USA, in 2009, and the M.S. and Ph.D. degrees in electrical and computer engineering from the University of California, San Diego (UCSD), CA, USA, in 2011 and 2014, respectively.

He is currently the Research Staff with the Applied Electromagnetics Laboratory, HRL Laboratories where he started in 2014. In 2010, he joined the Applied Electromagnetics Group, UCSD where he studied anisotropic artificial impedance surfaces as a Graduate Student Researcher. He is a member of Tau Beta Pi and Sigma Xi.

Daniel F. Sievenpiper (M'94–SM'04–F'09) received the B.S. and Ph.D. degrees in electrical engineering from the University of California, Los Angeles, CA, USA, in 1994 and 1999, respectively.

He is currently a Professor with the University of California, San Diego, where his research focuses on antennas and electromagnetic structures. Prior to 2010, he was the Director of the Applied Electromagnetics Laboratory, HRL Laboratories, Malibu, CA, where his research included artificial impedance surfaces, conformal antennas, tunable and wearable antennas, and beam steering methods. He has more than 70 issued patents and more than 80 technical publications

Dr. Sievenpiper has served as an Associate Editor of the IEEE ANTENNAS AND WIRELESS PROPAGATION LETTERS, since 2010. He currently serves as the Chair of the IEEE Antennas and Propagation Society Committee on New Technology Directions. In 2008, he was the recipient of the URSI Issac Koga Gold Medal.